Journal of Magnetic Resonance 278 (2017) 67–79

Contents lists available at ScienceDirect

Journal of Magnetic Resonance

journal homepage: www.elsevier.com/locate/jmr

Broadband quantitative NQR for authentication of vitamins and dietary supplements

Cheng Chen [a], Fengchao Zhang [b], Swarup Bhunia [b], Soumyajit Mandal [a,*]

[a] Case Western Reserve University, Cleveland, OH 44106, USA
[b] University of Florida, Gainesville, FL 32611, USA

ARTICLE INFO

Article history:
Received 13 January 2017
Revised 12 March 2017
Accepted 20 March 2017
Available online 24 March 2017

Keywords:
NQR
Broadband front-end
Quantitative measurement
Authentication

ABSTRACT

We describe hardware, pulse sequences, and algorithms for nuclear quadrupole resonance (NQR) spectroscopy of medicines and dietary supplements. Medicine and food safety is a pressing problem that has drawn more and more attention. NQR is an ideal technique for authenticating these substances because it is a non-invasive method for chemical identification. We have recently developed a broadband NQR front-end that can excite and detect ^{14}N NQR signals over a wide frequency range; its operating frequency can be rapidly set by software, while sensitivity is comparable to conventional narrowband front-ends over the entire range. This front-end improves the accuracy of authentication by enabling multiple-frequency experiments. We have also developed calibration and signal processing techniques to convert measured NQR signal amplitudes into nuclear spin densities, thus enabling its use as a quantitative technique. Experimental results from several samples are used to illustrate the proposed methods.

1. Introduction

The use of dietary supplements (DS) is widespread in the general population, and is often driven by the belief that they confer health benefits. According to a recent review [1], 52% of the participants in a survey reported using at least 1 type of supplement and 31% reported using multiple supplements. Although consumers expect that supplements purchased are effective and contain no harmful ingredients, some reports reveal that this is not always the case. Evidence of poor quality control in the manufacture and storage of supplements has been repeatedly reported in the past few years, with typical examples being poor quality and fraudulent practices [2]. A review of protein supplements from ConsumerLab reported that out of 24% commercially available protein supplement products, 32% failed the quality assurance test [3]. A more significant concern has been raised by the Food and Drug Administration (FDA): undeclared allergens, microbiological contaminants, and/or foreign objects are present in a wide range of supplement products [4]. Moreover, in cases where relatively expensive ingredients are involved, some products contain little or no active ingredients, e.g., melamine is used as a low-cost substitute for expensive protein ingredients [5,6].

Spectroscopic techniques are effective at evaluating the quality of agricultural and pharmaceutical products. These methods are desirable because of their minimal sample preparation requirements, which enables rapid analysis. Some of the most mentioned techniques include near-infrared spectroscopy (NIR), mid-infrared spectroscopy (Mid-IR), and Raman spectroscopy [7–9]. Nuclear magnetic resonance (NMR) is also widely used for measurements of liquids [10]. However, most vitamins and dietary supplements are sold in solid pill or powder form. Obtaining quantitative information about such samples from IR and Raman spectroscopy is challenging because these optical methods are sensitive to surface properties and packaging, while solid-state NMR requires expensive sample spinning equipment to obtain high-resolution spectra. On the other hand, nuclear quadrupole resonance (NQR) shows excellent performance in characterizing solid samples. The aforementioned analytical techniques are summarized in Table 1.

Several research groups around the world have investigated applications of ^{14}N NQR in detecting explosives and illegal drugs, both of which generally contain significant amounts of nitrogen [11–13]. The technique is of interest because the ^{14}N nucleus is quadrupole-active, has almost 100% natural abundance and is present in most of the drug and supplement products on the market. Moreover, it results in resonance frequencies that are highly dependent on molecular geometry. As a result, even closely-related molecules generally have widely-separated NQR lines,

* Corresponding author.
E-mail addresses: cxc717@case.edu (C. Chen), fzhang67@ufl.edu (F. Zhang), swarup@ece.ufl.edu (S. Bhunia), sxm833@case.edu (S. Mandal).

http://dx.doi.org/10.1016/j.jmr.2017.03.011
1090-7807/

Table 1
Comparison of analytical techniques suitable for solid supplements.

	Near-Infrared (NIR)	Mid-IR	Raman	NQR
Measured properties	Bond vibrations	Bond vibrations	Bond vibrations	Change of nuclear spin
Information obtained	Organic bond types and physical structure	Organic bond types and physical structure	Organic bond types and physical structure	Atomic and molecular structure and mobility
Resolution	Low	Medium	Medium	High
Sensitivity	Low	High	Medium	Low
Cost	Low	Relatively expensive	Relatively expensive	Low
Speed	Fast	Relatively fast	Relatively fast	Relatively slow
Result interpretation	Requires chemometrics	Comparison of spectrum	Comparison of spectrum	Comparison of spectrum
Non-Destructive	Yes	Yes	Yes	Yes
Sample type	Solids, liquids, powders, gels	Solids, liquids, powders, gels	Solids, liquids, powders, gels	Solids, powders
Container limit	Glass container	Glass container	Glass container	None

which improves the accuracy with which samples can be identified and the contents of mixtures quantified.

Like NMR spectrometers, the electronics system used for NQR also consists of a transmitter, a receiver, and one or more coils. Since maximum power transfer occurs when the source impedance is matched to that of the load, impedance matching is required on both ends of the transmission line connecting the transmitter and receiver to the coil. A passive impedance matching network is generally used to achieve both efficient RF power transmission and low-noise reception. However, such networks are inherently narrowband, so traditional NQR spectrometers have to be re-tuned to handle different spectral lines or different compounds. The issue limits the application of NQR in many practical situations.

In this paper, we remove the restriction by developing an electronically-tunable matching network that can operate over a wide range of frequencies. It has all the advantages of a single-tuned matching network, such as high efficiency, ease of design and construction, ease of debugging and repair, low cost, etc. Moreover, it can rapidly adjust its matching frequency through digital control pins that are set within the pulse program, which significantly extends its range of application. In particular, the transition between different frequencies is short enough to enable multi-frequency transfer experiments; it also allows us to interleave multiple pulse sequences to reduce overall experiment time. We take advantage of the tunable matching network and demonstrate its operation in several experiments including quantitative measurements, cross-polarization experiments, and two-frequency experiments. We also compare the results with theoretical calculations.

This paper is organized as follows. In Section 2 we describe the tunable matching network and the foundations of NQR. We also introduce the mathematical derivation of quantitative NQR-based measurements of sample properties. In Section 4, we demonstrate and discuss the experimental results. Finally, conclusions and suggestions for future work are presented in Section 5.

2. NQR theory

2.1. Matching network

Non-resonant (broadband) probes have been successfully used to replace narrowband impedance matching networks for NQR and low-field NMR [14,13]. Such non-resonant probes are completely impedance-mismatched, so almost all the power delivered by the transmitter is reflected back from the coil instead of being absorbed. Hence the supply voltage has to be significantly larger than for a traditional tuned probe to deliver the same current to the coil. This makes it difficult to run the system off batteries, which are preferable for their low noise and portability. Moreover, the probe is also impedance-mismatched during reception, which makes it necessary to use an ultra-low-noise preamplifier to get acceptable noise figure (NF). In this paper we focus on a tunable impedance-matched probe, which provides most of the benefits of a truly broadband probe without the attendant disadvantages.

We focus on the classic two-capacitor impedance matching network. The efficiency of this network is defined as the ratio of power delivered to the coil to total input power. It can be written as a function of frequency $\eta(f) = P_{coil}(f)/P_{in}(f)$. In addition, the input impedance of the network is given by

$$Z_{in}(\omega) = \frac{1}{j\omega C_2} + \frac{(j\omega L + R)\frac{1}{j\omega C_1}}{(1-\omega^2 LC_1) + j\omega RC_1}, \quad (1)$$

where C_1 is the capacitor in parallel with the coil and C_2 is the capacitor in series with the coil. The equation shows that the impedance does not increase monotonically with frequency. For the purpose of swiftly tuning and covering a wide range of frequencies, a multi-channel circuit was designed, in which C_1 and C_2 were divided into eight and six channels respectively. The capacitor values were approximately binary-weighted along the channels and controlled digitally by switches, thus resulting in a effective capacitance tuning range of approximately $1:2^8$ and $1:2^6$, respectively.

The properties of the switches are crucial for the experiments. Their figure of merit (FOM), which is generally defined as the product of on-state resistance (R_{on}) and off-state capacitance (C_{off}), directly determines the performance of the matching network and therefore influences the quality of experiments. We can choose switches from a variety of commercial devices. Mainly they can be categorized into two different types: electromechanical and solid state switches. In the former category, PIN diodes are current-controlled devices that are specifically developed for RF use. They have low R_{on} and C_{off} (i.e., low FOM) and high switching speeds, making them the preferred choice for switching RF power. However, PIN diodes do not work well at frequencies lower than $1/\tau_t$, where τ_t is the transit time through the device. At these frequencies, they behave like PN-junction diodes that distort the RF signal in both the "on" and "off" states due to voltage-dependent resistance and capacitance, respectively.

Another option is FET switches, which depend on an electric field to control the conductivity of a channel in the semiconductor, and thus achieve "on" and "off" states. FET switches consume much less current than PIN diodes because they are voltage-controlled devices. However, they have relatively high C_{off} which makes it difficult to precisely tune the matching network. Obviously hybrids of PIN diodes and FETs are not beneficial either because of the same capacitance problem. Hence we used electromechanical switches, which have very low FOM (about 100× lower than FETs), in our matching network. In particular, they have very low C_{off}, which is crucial for accurate tuning of the network. They do have a relatively slow response time of ~100 μs, but this

is tolerable in our application because the gaps between RF pulses are several hundred μs long. Another potential drawback of electromechanical switches is that they are affected by ambient magnetic fields. Fortunately, NQR, unlike NMR, does not require an external magnetic field.

In particular, we used miniature reed relays as the switches. These devices have physical contacts that are mechanically actuated to open or close a conducting path. They contain a solenoid coil that surrounds two movable cantilevers (also known as reeds). Current in the coil exerts force on the reeds, drawing them together to make the contact. After the coil current stops, the spring in the reed pulls the contacts apart and opens the circuit. Although reed relays are suitable for this application, there are some issues we need to pay attention to, such as power loss and current limit, which will be discussed in detail in the experimental setup section.

2.2. Population transfer experiments

One of the most common pulse sequences used for NQR experiments is known as the spin-locked spin echo (SLSE). It consists of an initial excitation pulse and a long train of refocusing pulses separated by the echo period t_E as shown in Fig. 1. Both the excitation pulse and the refocusing pulses have the same length but there is a relative phase shift of $\pi/2$ between them.

Population transfer experiments in NQR use a perturbation pulse to change the populations of the nuclear energy levels before pulses at another frequency (typically forming a SLSE sequence) are applied to generate coherences between two of these levels. The intensity of the resultant signal is proportional to the population difference between the levels, and is thus affected by the perturbation pulse.

Spin-1 nuclei such as ^{14}N have three stationary energy levels in the absence of an external magnetic field. Transitions between these levels result in three NQR resonances. The corresponding frequencies are conventionally denoted by ω_+, ω_-, and $\omega_0 = \omega_+ - \omega_-$. These frequencies can also be written as

$$\omega_\pm = \frac{3\omega_Q}{4}\left(1 \pm \frac{\eta}{3}\right),$$
$$\omega_0 = \omega_+ - \omega_- = \frac{\eta\omega_Q}{2}. \tag{2}$$

Here ω_Q is known as the quadrupole coupling constant and $0 \leqslant \eta \leqslant 1$ is the asymmetry parameter. The expected changes in amplitude caused by the perturbation pulse can be theoretically calculated [15]. Hence we can indirectly measure an NQR transition by observing signals produced by another transition. This method also improves the credibility of positive signals by eliminating the false signals induced by external interference [13].

Most previous multi-frequency population transfer experiments have used mutually orthogonal transmit and receive coils [16,15]. However, for powder samples some effects can also be observed with a single coil [13], which simplifies the experimental setup. We applied a multi-frequency pulse sequence which has been commonly used in pulsed NQR. It is shown in Fig. 2. An initial pulse functions as a perturbation which manipulates the second NQR transition at a different frequency. The part within the brackets is repeated N_E times to produce multiple spin echoes for the purpose of increasing signal-to-noise ratio (SNR). The delay between the first and second pulses should be much shorter than T_1, i.e. $\tau \ll T_1$, to avoid signal loss due to relaxation. Since the populations of the ^{14}N energy levels are coupled, the NQR signal amplitude will change when a second transition is saturated by the first pulse.

A detailed theoretical derivation of the resultant NQR signal amplitudes has been presented in [13] based on the assumption that the separation between the two resonant frequencies greatly exceeds the excitation bandwidth, and the results are summarized in the matrix below. The rows denote the perturbation frequency $\omega_{RF,1}$ and the columns denote the excitation frequency $\omega_{RF,2}$. The values show the detected signal amplitude when a perturbation pulse of nominal flip angle θ_1 is applied, normalized to the case when $\theta_1 = 0$ (i.e., no perturbation pulse).

$$\frac{s(p,q)}{s_0(p,q)} = \begin{bmatrix} \cos(\theta_1 a) & \frac{3(1-\eta)+(3+\eta)\cos(\theta_1 a)}{2(3-\eta)} & \frac{-3(1-\eta)+(3+\eta)\cos(\theta_1 a)}{4\eta} \\ \frac{3(1+\eta)+(3-\eta)\cos(\theta_1 b)}{2(3+\eta)} & \cos(\theta_1 b) & \frac{3(1+\eta)-(3-\eta)\cos(\theta_1 b)}{4\eta} \\ \frac{3+\eta\cos(\theta_1 c)}{3+\eta} & \frac{3-\eta\cos(\theta_1 c)}{3-\eta} & \cos(\theta_1 c) \end{bmatrix}. \tag{3}$$

Here $\theta_1 \equiv t_{p1}\omega_{1,1}$ and $\theta_1 \equiv t_{p2}\omega_{1,2}$ are the nominal flip angles of the pulses, and $\omega_{1,1}$ and $\omega_{1,2}$ are the nutation frequencies of the first and second pulses. Furthermore, a, b, and c are projection functions of the Euler angles α and β, and are equal to $\cos(\alpha)\sin(\beta), \sin(\alpha)\sin(\beta)$, and $\cos(\beta)$ respectively. Note that Eq. (3) predicts the results for a particular Euler angle, i.e. for a particular crystallite. However, the coefficients are different for different crystallites in a powder sample. Hence we need to average the angles over all the crystallites in the sample to estimate the signal amplitude. The averaged signal can be calculated in spherical coordinates as follows:

$$s_{av}(t) = \frac{1}{4\pi}\int_0^{2\pi}\int_0^{\pi} s(\alpha,\beta,t)\sin(\beta)d\beta d\alpha. \tag{4}$$

The same powder average integral will later be used to estimate the $s_{exc}(\theta)$ nutation function, which in turn is required to estimate the NQR signal amplitude.

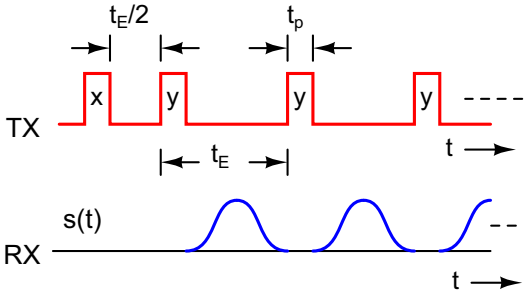

Fig. 1. Basic spin-locked spin echo (SLSE) pulse sequence used for NQR experiments, and the resulting received signal $s(t)$.

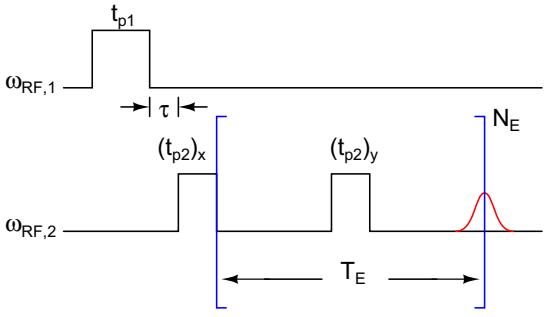

Fig. 2. Two-frequency $(\omega_{RF,1}, \omega_{RF,2})$ pulse sequence with SLSE signal detection. The delay after the initial pulse provides transition time between the two frequencies, but should be much smaller than T_1. The part between the blue brackets is repeated N_E times to obtain a sequence of echoes.

3. NQR signal estimation and processing

3.1. NQR signal estimation

In a SLSE sequence, NQR signals are acquired between refocusing pulses and averaged over several scans to improve the SNR. The amplitude of each spin echo can be estimated by integrating the acquired signals with a weighting or window function; the optimum window function in the presence of additive white Gaussian noise (AWGN) is known to be the complex conjugate of the expected echo shape. The signal amplitude is dependent on several factors. In particular, it is proportional to the total number of active nuclei, allowing NQR to be used for quantitative analysis of mixtures. However, it is critical to derive an accurate theoretical relationship between these quantities in order for NQR to obtain reliable quantitative results that ensure trustworthy analysis of unknown samples. The necessary mathematical relationship can be estimated in several steps, as shown in Fig. 3.

Following the steps in Fig. 3, we can estimate N_s, the total number of nuclei of the species of interest within the sample as follows:

$$N_s = \frac{s_a(0,0)}{G(\omega_0)}\sqrt{\frac{R_{coil}}{Z_0}}\frac{6kT_s}{\gamma\hbar^2\omega_0^2}\left[\frac{l_s}{\int_{-l_s/2}^{l_s/2} s_{exc}(\theta(x))\left(\frac{B_1(x)}{I_1}\right)dx}\right]. \quad (5)$$

Here $s_a(\delta t, kT_E)$ represents the k-th time-domain echo after windowing, with δt being the signal acquisition window $-t_{acq}/2 < \delta t < t_{acq}/2$ and T_E being the echo period. Thus, $s_a(0,0)$ represents the peak echo amplitude extrapolated to $t = 0$. In addition, $G(\omega)$ is the voltage gain of the receiver, R_{coil} is the series resistance of the coil, Z_0 is the matched impedance, γ is the gyromagnetic ratio, $\hbar$ is Planck's constant, ω_0 is the resonant frequency, and kT_s is the product of the Boltzmann constant and sample temperature. Finally, $\theta(x) \equiv \gamma B_1(x)t_p$, $s_{exc}(\theta)$ is a response function that consists of the NQR nutation curve $s_{exc}(\theta)$ weighted by $B_1(x)/I_1$, which is the RF magnetic field amplitude B_1 generated per Ampere of current in the coil. The latter is a position-dependent measure of coupling strength between the coil and the sample, and l_s is the length of the sample. The detailed derivation of Eq. 5 is shown in Appendix A.

3.2. Matched filtering for white noise

A matched filter is essential in low-power experiments to optimize the SNR and make the received signal suitable for detection. The expected echo amplitudes (y_s) after matched filtering in the presence of frequency-independent ("white") additive Gaussian noise are given by:

$$y_s(kt_E) = e^{-kt_E/T_{2,eff}}\sqrt{\int_{-\infty}^{+\infty}|s_a(\tau,0)|^2 d\tau}. \quad (6)$$

A detailed derivation of Eq. 6 is provided in Appendix B. The value of $y_s(0)$ is solely dependent on $\sqrt{\int_{-\infty}^{+\infty}|s_a(\tau,0)|^2 d\tau}$, which is the root-mean-squared (rms) amplitude of the acquired echoes at $t = 0$. Note that this quantity is in general different from the peak echo amplitude $s_a(0,0)$ used in Eq. (5). The rms amplitude has the highest possible SNR but is dependent on T_2^* (and thus the linewidth); the peak amplitude has lower SNR but is independent of T_2^* (and thus more suitable for directly estimating the number of nuclei N_s in the sample). It is also worth noting that the rms amplitude estimation procedure described above requires the SLSE decay time constant $T_{2,eff}$ to be known. For unknown samples, an iterative procedure is thus necessary, as summarized below:

1. Perform matched filtering with an initial guess for $T_{2,eff}$.
2. Numerically fit the resulting decay curve $y_s(kt_E)$ to obtain an updated estimate for $T_{2,eff}$.
3. Repeat steps 1–2 until $T_{2,eff}$ converges to a fixed value.

In most cases, only 2–3 iterations are required. A flow chart describing the entire procedure is shown in Fig. 4. It can be easily generalized to multi-exponential decays.

3.3. Matched filtering for non-white noise

The theory in the last section cannot be directly applied to narrowband probes, since they do not exhibit white Gaussian noise. Moreover, external sources of radio-frequency interference (RFI) do not generate white noise either. The matched filter can be modified to account for this fact. It can be shown that the new optimum solution is to use an additional "whitening" filter $H_W(\omega)$ in front of the usual matched filter we have already described. The resulting optimal signal amplitude (y_M) is given by:

$$y_M = N_{out}\int_{-\infty}^{\infty}|SNR(\omega)|^2 d\omega. \quad (7)$$

A detailed derivation of Eq. 7 is provided in Appendix B. The optimally-detected signal amplitude is purely real, and is proportional to the integral of the expected signal-to-noise ratio (SNR) in power units as a function of frequency. This is a generalization of our earlier result for white noise. In that case SNR was simply proportional to the PSD of the signal, since the PSD of the noise was defined to be constant.

The effects of colored noise become important when the bandwidth of the probe is comparable or smaller than that of the signal, i.e., in narrowband probes where $BW_{probe} \leqslant BW_{signal}$. In such cases, the noise PSD at the receiver varies significantly across the signal bandwidth. Such effects are important for high-Q probes at low frequencies, and also when broadband pulse sequences increase the bandwidth of the NQR signal.

3.4. Variance estimation

Estimation of variance is crucial for quantitative measurements, since variance in the received signal due to noise, time-varying RF interference, etc. directly affects the reliability of the measurement. In particular, the amount of active ingredient in a pharmaceutical product must lie within a certain range in order to pass quality control; given a certain amount of sample, the measurement variance has to be small enough to keep false positive and false negative rates below acceptable levels.

In non-ideal situations, it is likely that individual NQR experiments will be conducted in slightly different conditions. It may be necessary to reduce such measurement uncertainty by controlling the sample temperature and/or shielding the sample coil. In

Fig. 3. Theoretical calculation from spin density to received voltage. The numbers on the arrows represent corresponding equations in the paper (including the appendices).

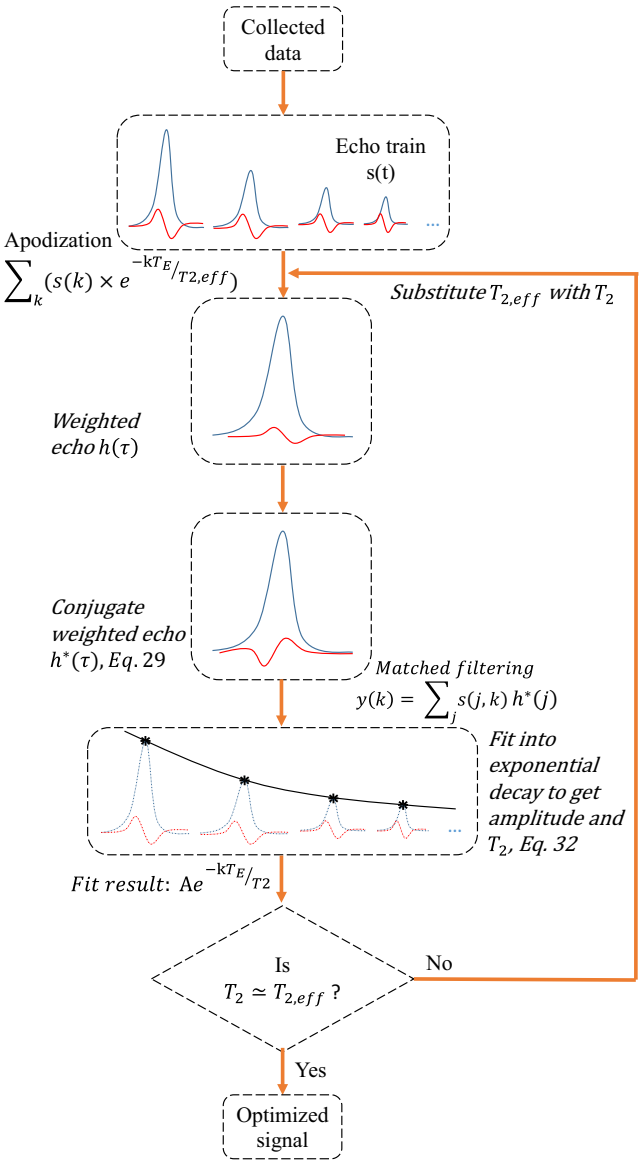

Fig. 4. Flow chart describing the SNR optimization procedure. Two levels of matched filtering/apodization are applied to the time-domain signal. One is applied to individual echoes, while the other is applied to the entire echo train. The result is then numerically fitted to extract the initial signal amplitude A and decay rate $T_{2,eff}$. The entire process is repeated until $T_{2,eff}$ converges to a fixed value.

any case, let us assume that we have collected data from one or more samples of interest. The next step is to quantify the variance of the measurements. One possibility is to use a second coil to measure the background noise. Another is to directly estimate the noise from the received data. For example, if the matching network has much greater bandwidth than the NQR linewidth, one can assume that regions of the acquired spectra that are far away from the signal arise from background noise. Furthermore, if we assume that the noise arises from a stationary process, we can estimate its statistical properties (mean and variance) from the recorded data and then create artificial noise with the same properties. For example, if the variance is dominated by white noise, it is generally well-fit by a Gaussian distribution. Such artificial noise is then added to the estimated signal decay curve and fed into the matched filtering and fitting algorithm described earlier, and the resulting values of initial signal amplitude $s_a(0,0)$ and decay constant $T_{2,eff}$ recorded. The process is repeated 100 or more times to enable the distributions of these output parameters to be reliably estimated. In this way we can estimate experimental variance from the data acquired during a single measurement, thus minimizing the overall measurement time.

4. Experiments

4.1. Experimental setup

The experiments used a single solenoidal excitation and detection coil. We made the coil by winding AWG 20 wire around a hollow PVC cylinder. The cylinder was 75 mm tall in total with a 10 mm high base. Its outer surface was machined with a thread, which enables the coil to be wound tightly on the former and then glued on to get stable results. The solenoid consisted of 38 turns with an effective diameter and length of 32 mm and 60 mm, respectively. The cylinder was then mounted along with the matching network inside a aluminum box to reduce RF interference (see Fig. 5). A commercial desktop MR spectrometer (Kea 2, Magritek) with a graphical software interface was used to generate pulse sequences and receive the data.

Individual capacitor channels in the matching network can be triggered to be turned "on" and "off" from the NQR pulse sequence as shown in Fig. 6. The spectrometer generates logic-level pulses on a single line. Rising edges of this waveform are counted by an accumulator on the matching network PCB. The output bits of the accumulator serve as a binary representation of the number of input pulses, and are then used to switch the state of individual capacitors as shown in the figure. This series-to-parallel digital conversion scheme enables us to work around the limited number of programmable digital output lines (8 in this case) provided by the spectrometer.

As we have mentioned, the impedance of the matching network does not increase monotonically with frequency. Moreover there are a total of $2^8 \times 2^6$ potential combinations of capacitors for generating matching frequencies. If we do not eliminate some of these combinations, it will be very time-consuming to find the right values. Empirically to get minimum reflection at a particular frequency, the value of C_1 is usually 2–8 times bigger than the value of C_2. As a result, we can just search through the values

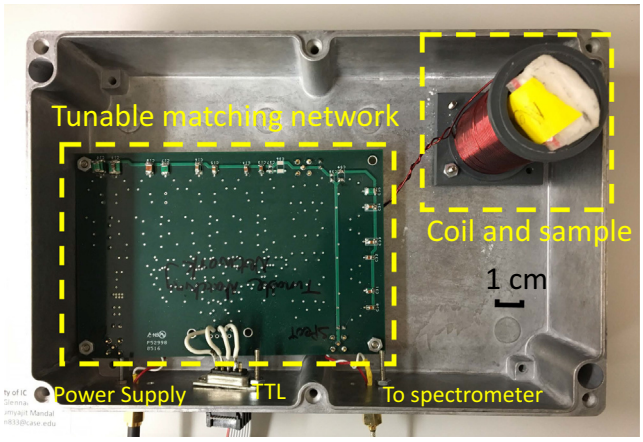

Fig. 5. Experimental setup for the tunable matching network. The matching network board was fabricated by a commercial vendor, while the probe holder was fabricated in-house. Both of them were placed in an aluminum enclosure to reduce RFI. Most of the programming-related components on the board were soldered on the bottom to prevent interference with RF components (the capacitors), which were soldered on the top; the two sides were electrically isolated by a ground shield on the board. A 6 V motorcycle battery was used as the power supply, and TTL-level digital signals were applied to assign "on" and "off" states to the channels.

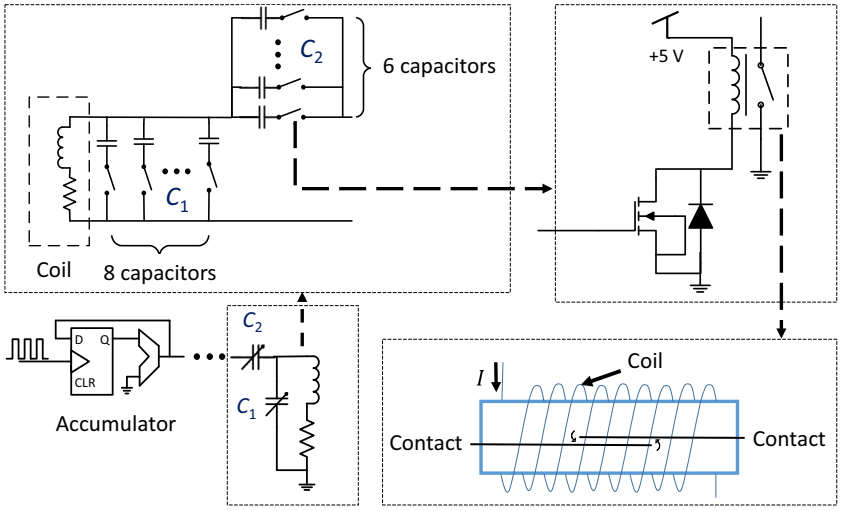

Fig. 6. Tunable matching network schematic. Left bottom: A series of pulses are generated by the spectrometer and enter a shift register, which then assigns bits to corresponding channels to realize the calculated capacitor value. Left top: Eight parallel and six series capacitors with calculated values realize the matching network. Left bottom: Schematic of an individual channel. A MOSFET acts as a switch in series with the relay coil. When it is in the "on" state, it enables the relay, thus connecting the capacitor in this channel to the circuit. Right bottom: The structure of a single relay. When there is current flowing into the coil, an internal magnetic field is created, which forces the two reeds together to create a conducting path.

around those ratios, and skip the obviously unreasonable combinations.

Experimentally, the digitally-controlled impedance matching network allowed us to operate over a wide frequency range (1–3 MHz). The lower limit is determined by the spectrometer's tuned duplexer circuit, and can be decreased by using a broadband switch-based duplexer [14]. The upper limit is determined by the onset of self-resonance in the sample coil. We chose miniature reed relays (9901, Coto Technology) as the switches; they switch quickly compared to other relays ($\sim 250\,\mu s$ to turn "on", and $\sim 50\,\mu s$ to turn "off"), and are also suitable for mounting on printed circuit boards (PCBs). Simulations based on the coil's measured inductance and series resistance were run to obtain a rough estimate of the lowest and highest C_1 and C_2 values needed. We then implemented the capacitors by carefully choosing combinations of mica capacitors to realize binary-weighted values, thus ensuring that the matching network is able to tune smoothly over the whole range. Fig. 7(a) demonstrates measured reflection coefficients produced by the selected capacitor combinations. Frequency-dependent insertion loss from the spectrometer's duplexer has been removed for clarity.

The performance of the proposed matching network is limited by several factors. Firstly, the programmed circuit is able to provide a good match at the desired RF frequency in most cases. However, in some cases the spacing between adjacent network states is too coarse to provide good matching; this usually occurs for relatively narrowband excitation (long pulses) towards the upper end of the frequency range. In addition, at higher frequencies, changes in the resonant frequency due to temperature drifts also affect the matching performance. Secondly, we are limited by the spectrometer's built-in duplexer, as mentioned previously. The latter was designed to operate in the 2–5 MHz range, and suffers from increasing insertion loss below 2 MHz – at this frequency the insertion loss is already over 1 dB, which is a 25% loss in power. Below 1 MHz the loss increases dramatically, making it impossible to detect any signals. Thirdly, the maximum switching current and voltage ratings of the relays limit the power handling capability of the network. The current and voltage limits (denoted by P_V and P_I, respectively) can be described in terms of the input RF power level as follows:

$$P_V = \frac{1}{2} V_{max}^2 \frac{R_s}{(\omega L_s)^2 + R_s^2},$$
$$P_I = \frac{1}{2} I_{max}^2 \frac{R_s}{(\omega L_s)^2 + R_s^2} \frac{1}{(\omega C_{total})^2}. \quad (8)$$

Here C_{total} is defined as

$$C_{total} = \sum (C_{i,on} b_i + C_{i,off} \bar{b}_i), \quad (9)$$

where b_i represents the bits that are in the 'on' state, and L_s and R_s are the series inductance and resistance of the coil, respectively. For the original relays, the current limit is 0.5 A while the voltage limit is 160 V. Fig. 7 shows the relationship between allowed power limit and frequency for the two constraints defined in Eq. (8). These constraints can be improved by switching to relays with higher voltage and current limits. An example is the Coto 9290, which has 2× higher current and voltage ratings at the cost of a somewhat larger form factor. Fig. 7(b) shows the resulting maximum input power level that can be safely handled by the tunable matching network as a function of frequency for both types of relay. It is interesting to note that the voltage and current limits shown here are highly conservative values provided by the manufacturer. In our experiments, the relays handled ∼4× higher power levels without any hardware failures.

Another issue worth paying attention to is the amount of power lost in the matching network, since the resulting resistance directly affects SNR. The chosen relay has $C_{off} \approx 1$pF and $R_{on} \approx 0.2\,\Omega$. We can calculate the effective quality factor of the coil ($Q = \omega_0 L_{coil}/R_{coil}$) after taking these parasitic elements into account. The result is shown in Fig. 7(c). We see that the matching network degrades Q by about 30%, which corresponds to a 15% decrease in SNR. Finally, since the relays need $\sim 250\mu s$ to turn 'on', we have to wait up to ∼1 ms until the circuit settles to a new matching frequency.

4.2. Quantitative measurements

As we have discussed in the theoretical analysis section, NQR is a volumetric measurement; the signal amplitude is directly

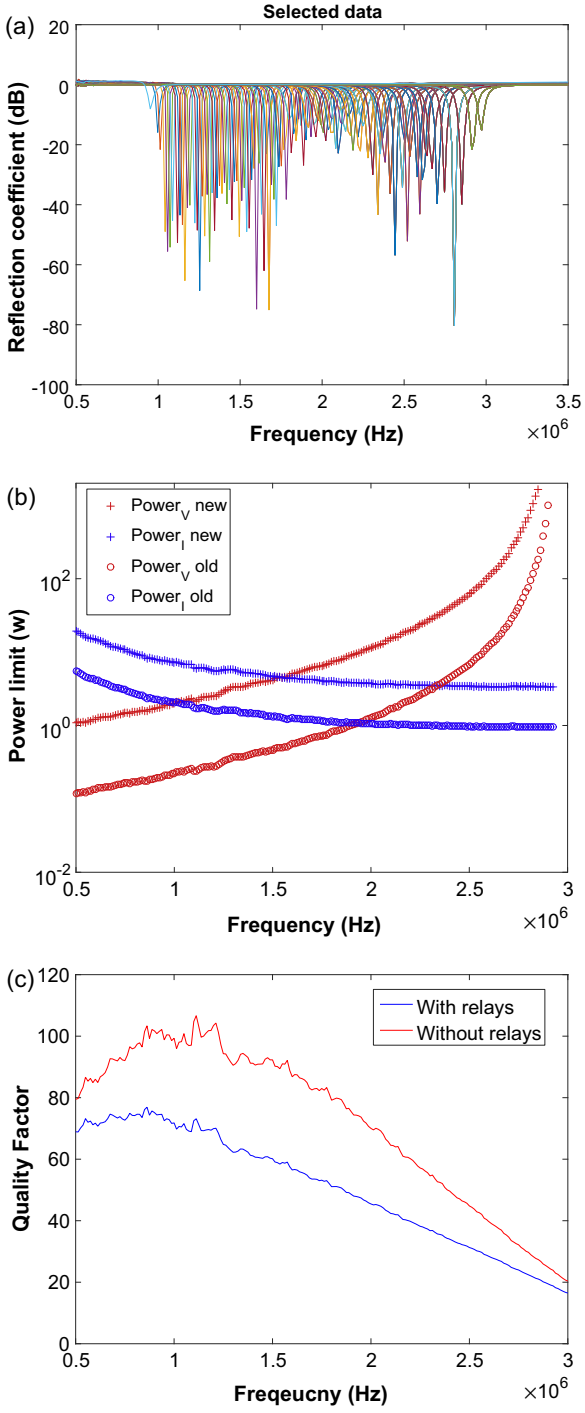

Fig. 7. (a) Selected resonant frequencies in the range of 1–3 MHz. The insertion loss of the duplexer has been removed while drawing this plot. (b) Maximum acceptable input power determined by current and voltage limits for the relays. The results for two commercially-available reed relays are shown: Coto 9901 ("old") and Coto 9290 ("new"). This plot shows that there is a stricter limit for voltage at higher frequencies and current at lower frequencies. The new relay has a looser power constraint. (c) Measured coil quality factor (Q) with and without the relays.

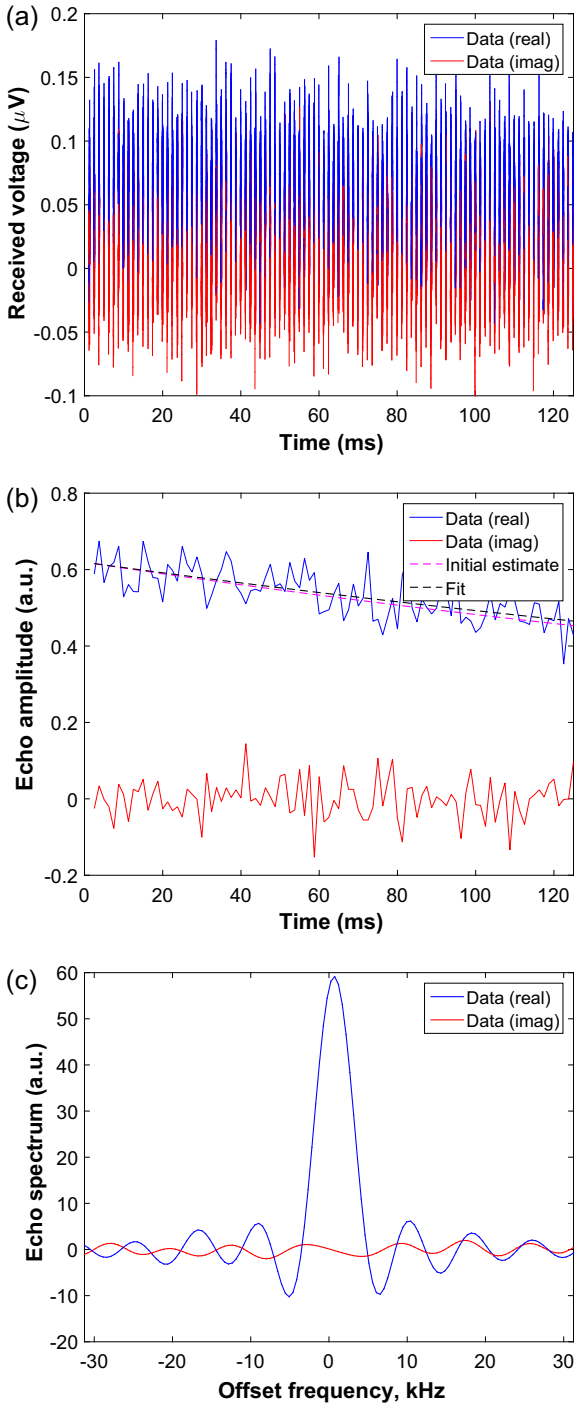

Fig. 8. Data from experiments with 30 g of melamine. (a) Raw echoes collected from the sample. (b) Echoes after matched filtering. The filtered echoes were fit to a mono-exponential decay function. The resulting value of $T_{2,eff}$ was 437 ms, while the SNR was 14.5 per scan. (c) Normalized frequency domain spectrum. The pulse length was 250 μs, the echo period was $t_E = 1250$ μs, the number of echoes was 100, the inter-scan time was 20 s, the acquisition time was $t_{acq} = 0.256$ ms, and the number of scans was 16.

proportional to the number of nuclei of test sample, making it possible to quantitatively analyze unknown samples.

As an example, we measured the amount of melamine in a powder sample. Melamine was previously reported to have been illegally added into milk powder for increasing its apparent protein content, and therefore its nitrogen content. The results are shown in Fig. 8. For 30 gm of 99% melamine from Sigma Aldrich, the first echo amplitude $s_a(0,0)$ is measured as 0.170 μV. The theoretical calculation described earlier predicts a signal amplitude of 0.212 μV, so agreement between theory and experiment is good. There is a significant amount of B_1 inhomogeneity across the sample (which has a length of ∼5 cm), as shown in Fig. 9. This results in ∼20% decrease in signal amplitude compared to a uniform B_1 field

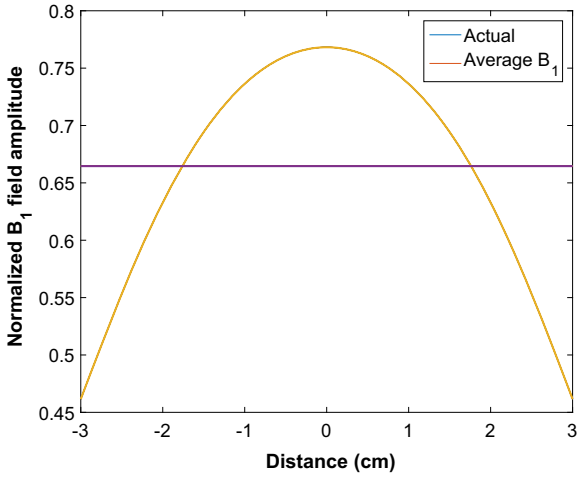

Fig. 9. The influence of B_1 field distribution is significant. The coil has a length of 6 cm and contains 38 turns. For a given sample volume, if we need to maximize the signal strength, it is preferable that the sample is placed in the central region of the coil where the B_1 field is relatively uniform.

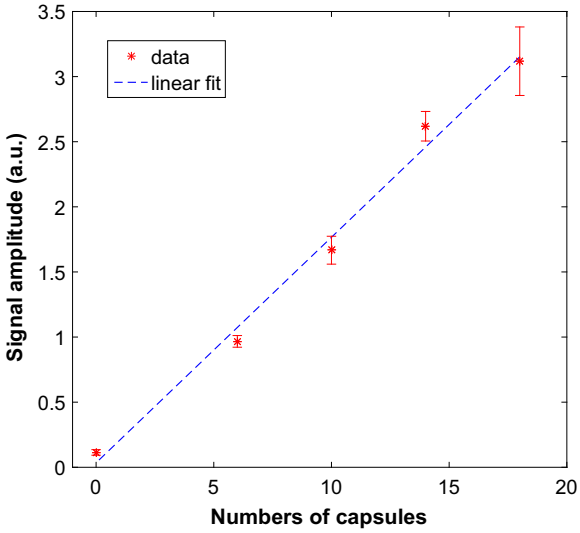

Fig. 10. Measured signal amplitudes shown as a function of the number of weight-loss drug capsules. Each capsule weighed 350 mg. The best-fitting value of $T_{2,eff}$ was about 4.3 ms, and the SNR was 0.08 per scan. The pulse length was 250 μs, the echo period was $t_E = 800$ μs, the number of echoes was 20, the inter-scan time was 2 s, and the acquisition time was $t_{acq} = 0.16$ ms. The data points were averaged over 10,240 scans. The total experiment time required for each sample point was approximately 4 h.

with the same maximum value. Field homogeneity can be greatly improved by using coils with non-uniform winding density [17,18].

In addition, we measured a weight-loss drug named "Phentramine Xtreme extra" that was purchased on eBay. The label on the product suggests that it contains 100 mg caffeine per 350 mg capsule. It is known that caffeine generates an NQR line around 2750 kHz; we used this line in our experiments. The experiment was performed using the device described in the previous section. A maximum of 18 capsules were found to fit inside the coil. We measured NQR spectra around the resonant frequency for different numbers of capsules ($N \leqslant 18$). The signals were significantly affected by temperature fluctuations, which causes the measured signals to fluctuate around the original resonant frequency. We have to compensate for this effect, i.e., remove the offset frequency, in order to get the correct echo shapes. After filtering, the acquired echoes were fit to a Gaussian function in the frequency domain. The mean of this function was then used to shift the acquired spectrum back to the original resonant frequency. The echoes were then integrated in the time domain to estimate the NQR signal amplitude. The entire procedure was repeated as a function of the number of capsules, and the results are shown in Fig. 10.

The result was then compared with data from pure caffeine. We tested a sample containing 24 gm 99% pure pharmaceutical-grade caffeine from Sigma Aldrich. The normalized signal amplitude measured from this sample was 12.96 with a variance of 0.25, compared to the normalized signal from 18 of the weight-loss capsules, which was 3.12 with a variance of 0.33. Assuming that the signal amplitude is linearly proportional to the quantity of caffeine, the quantity of caffeine per capsule is estimated to be 115 ± 12 mg, which is in agreement with the product label.

We also cross-referenced the caffeine results with ^{1}H NMR spectroscopy. The samples were prepared as follows: first, 0.2 gm of the contents of the capsules was extracted and fully dissolved into 30 ml of D_2O (99.9% purity). There was some precipitation, perhaps formed by the leftovers of crushed leaves used within the capsules. This might have reduced the amount of dissolved caffeine and thus slightly affected the accuracy of the experiment. Next, 0.2 gm of 99.9% pure caffeine was also dissolved into the same amount of D_2O. Both samples were inserted inside 5 mm NMR tubes. Simple ^{1}H experiments were then performed in a 500 MHz Bruker Ascend Avance HD^{TM} spectrometer provided with a two-channel Broadband Inverse probe. The results are shown in Fig. 11. The spectrum of pure caffeine contains four main peaks, which are also present in the spectrum of the weight-loss drug. Hence the presence of caffeine in the drug is confirmed. In addition, the drug spectrum contains peaks from other ingredients. By comparing the caffeine peaks in both spectra, we find that the ratio of the intensities is approximately 2.7. Based on this result, we estimate that each capsule contains approximately 129 mg of caffeine. Thus the NQR and NMR results are in agreement; the difference between the two measurements is nearly within the expected variance of the NQR experiment.

4.3. Cross-polarization experiments

An important limiting factor in NQR applications is that the signals are weak, which makes them vulnerable to corruption by RFI and also increases the time required to obtain a certain SNR. However, signal strengths can be significantly enhanced a polarization transfer technique [19]. The polarization source consists of nearby spins with a large gyromagnetic ratio, such as protons. These spins are pre-polarized in a static magnetic field generated either by a permanent magnet or an electromagnet. The field does not have to be particularly uniform, which makes low-cost and portable instruments easy to realize [20]. Cross-polarization occurs during adiabatic demagnetization of the sample when the proton Larmor frequency approaches any of the NQR frequencies. The enhanced NQR signal can then be detected in the usual way.

An example of measured data from melamine is shown in Fig. 12. The samples are all weighted mixtures of melamine and milk powder. The quantity of the melamine varies between different samples while the total sample weight is kept fixed at 4 gm. In each case, there is a significant amplitude increase when the sample is pre-polarized for 60 s in the 0.5 T field generated by a bench-top permanent magnet. The amount of enhancement ($\sim 4\times$) is in good agreement with theoretical estimates [21], and corresponds to a $\sim 16\times$ decrease in the time required to obtain a certain SNR. Moreover, the cross-polarized signal amplitudes show the same linear relationship versus amount of melamine as the non-cross-polarized ones, showing that this technique is suitable for

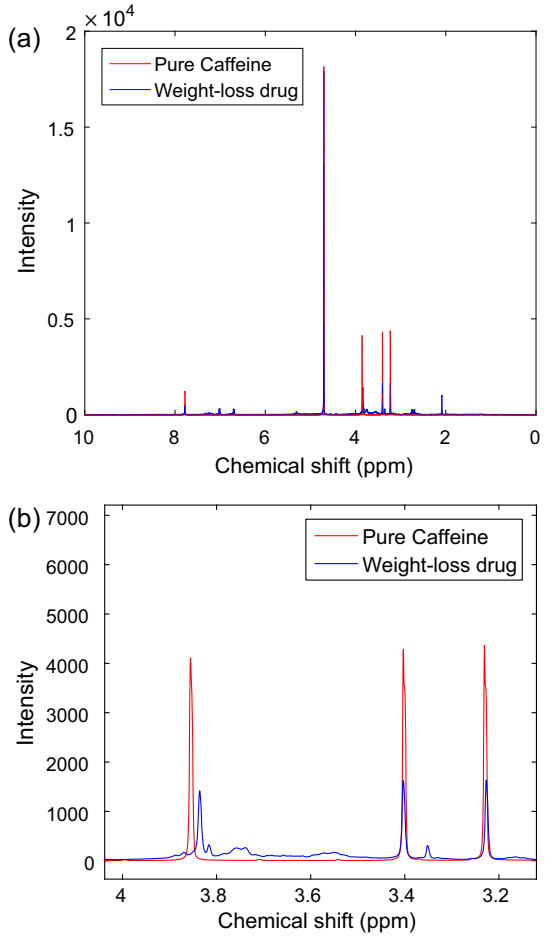

Fig. 11. (a) ^{1}H NMR spectra for pure caffeine and the weight-loss drug. The red line represents pure caffeine, while the blue line represents the weight-loss drug. The latter has more lines as expected. (b) Zoomed-in view of a particular spectral region. The average intensity ratio between pure caffeine and the weight-loss drug is around 2.7. (For interpretation of the references to color in this figure legend, the reader is referred to the web version of this article.)

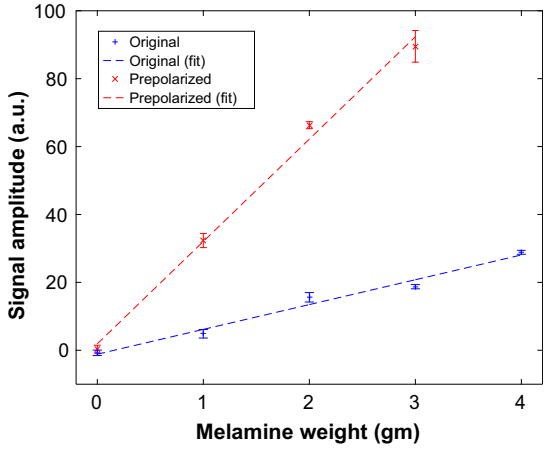

Fig. 12. Comparison between measured signal amplitudes from melamine mixtures with and without cross-polarization in a 0.5 T field. The signals are detected through the SLSE multi-echo pulse sequence.

quantitative experiments. Cross-polarization can thus play a very important role while analyzing unknown samples; it enables us to rapidly search a broad frequency range for possible NQR transitions. The amount of signal enhancement can be optimized by using a mechanized sample motion stage to precisely control the time course of adiabatic demagnetization.

4.4. Two-frequency experiment

The tunable matching network can perform two-frequency population transfer experiments by scanning both ω_{RF_1} and ω_{RF_2} of a particular site to locate the frequencies where signal increases or reduces. The fact that the phenomenon occurs only when the resonant frequencies are generated by the same nucleus provides useful information for identifying the contents of unknown mixtures [13]. Furthermore, it enables more robust and accurate measurements of complex mixtures, especially when the desired NQR line is located close to other lines and/or strong RFI. Fig. 13 illustrates simulated and measured signals for one of the six possible population transfer cases shown in Eq. (3). The sample was melamine, and powder averaging has been applied. In this case, the perturbation pulse decreases the signal amplitude; the first minimum occurs at 330°. The experimental data is in good agreement with the theoretical curve.

We also performed a frequency-swept population transfer experiment. The sample is 30 gm of 99% melamine from Sigma Aldrich. The quadrupole coupling constant $\omega_Q = 3313$ kHz and the asymmetry parameter $eta = 0.39$, resulting in $\omega_+ \approx 2809$ kHz and $\omega_- \approx 2160$ kHz. We scanned $\omega_{RF,1}$ around the ω_- resonance while keeping the detection frequency $\omega_{RF,2}$ fixed near the ω_+ resonance; this is the (ω_-, ω_+) case shown in Eq. (3). After powder averaging, this equation predicts ~12% drop in signal amplitude when $\theta_1 = 120°$ compared to the reference or unperturbed case ($\theta_1 = 0$).

The plot in Fig. 14 shows the measured results for $\theta_1 = 120°$. The signal amplitude detected at $\omega_{RF,2}$ shows a significant decrease of approximately 8% when $\omega_{RF,1}$ matches the resonant frequency, which is in agreement with the theoretical analysis. The result also confirms that the NQR lines at 2809 kHz and 2160 kHz originate from the same nucleus, i.e., a single site in the melamine molecule.

4.5. Key observations

The proposed device has shown its capability and effectiveness for authenticating vitamins and dietary supplements. The proposed

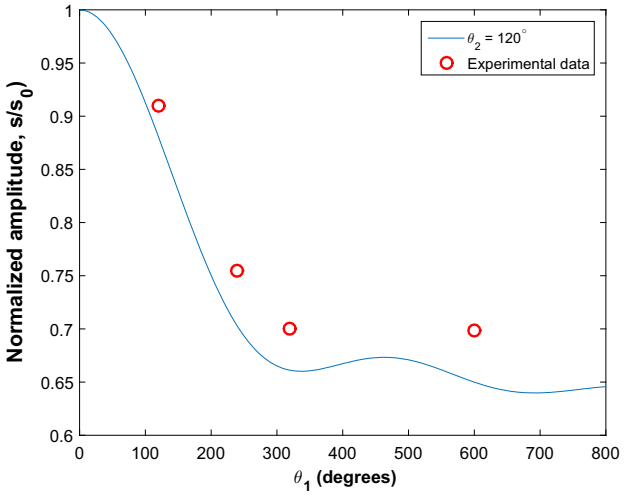

Fig. 13. Blue line: simulated NQR signal amplitude from a powder sample with $\eta = 0.39$ for the two-frequency pulse sequence as a function of the flip angle of the first pulse. Red circles: experimental data from melamine. (For interpretation of the references to color in this figure legend, the reader is referred to the web version of this article.)

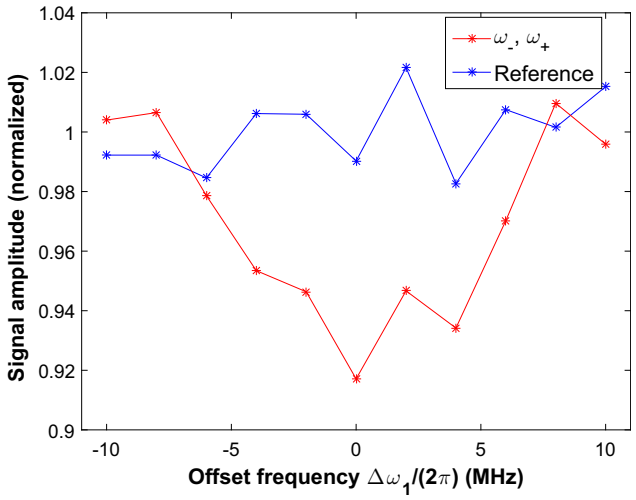

Fig. 14. Measured two-frequency SLSE amplitudes as a function of the initial pulse frequency. The sample was 30 gm of 99% melamine. The SLSE pulse length = 320 μs, echo spacing $t_E = 1250$ μs for $\omega_{RF,1} = \omega_-$, and 250 μs and 1250 μs respectively for $\omega_{RF,2} = \omega_+$. In addition, we used an initial delay of about 3 ms, and 64 scans.

hardware and enhanced NQR signal processing methods allow us to effectively determine the composition of these substances and hence, detect counterfeiting and mislabeled items. For instance, in the case of weight-loss drug, we were able to identify a minimum signal of 6 capsules within a few hours. With the help of cross-polarization, the minimum detectable sample volume will be further reduced.

The experiments show that the tunable matching network is capable of switching frequency rapidly in the desired range, although its tuning range and resolution can be further improved by adding more channels. A minor issue with the current design is that the on-board accumulator outputs are not latched during programming. As the channels are assigned to be turned on or off, some of them therefore go back and forth between "on" and "off" states multiple times before settling. This results in a longer settling time for the entire network. These issues will be solved in the next version of the matching network. Moreover, we found that long-term measurements (lasting longer than ~1 h) are significantly influenced by temperature drift. The acquired data has to be post-processed to compensate for such drifts, as described in the paper.

5. Summary and conclusions

We have introduced the use of a digitally-tunable probe for pulsed ^{14}N NQR. Our system is easy to program, robust, and capable of rapid frequency switching. This allows a variety of multi-frequency experiments. For example, the ability to operate efficiently over a broad frequency range allows the coupling between multiple NQR lines generated from a single site to be studied. Such coupling makes chemical identification more reliable by enabling unambiguous identification of NQR lines that arise from a single site and also reduces the rate of false positives in the presence of external RFI. Furthermore we discussed the theoretical basis of NQR-based materials authentication. In particular, we summarized the mathematical relationship between number of spins in the sample and measured voltage.

The work presented in this paper may be useful for both laboratory and commercial applications of NQR, such as studies of chemical structure and authentication of drugs and dietary supplements. In particular, potential applications to the field of dietary supplements are worth investigating. Moreover, it also has the potential to significantly speed up the experiments, to reduce the size and weight of the NQR device, and eventually make it portable.

Acknowledgments

The authors would like to thank Dr. Jamie Barras of King's College, London for interesting discussions and providing valuable experimental data for reference, Dr. Hope Barkoukis and Dr. Stephanie Harris of the School of Medicine, Case Western Reserve University for valuable insights and suggestions on nutrition and dietary supplements, and Kun Xu of Temple University, PA for grammar support. This work was partially funded by the National Science Foundation through grant CCF-1563688.

Appendix A. Derivation of Eq. (5)

The basic pulse sequences is shown in Fig. 1. It consists of an initial excitation pulse and a long train of refocusing pulses separated by the echo period t_E. The amplitude of the detected NQR signal in powder samples is a damped oscillatory function of the strength of the excitation. Thus, the response of the dynamical system to perturbations is strongly nonlinear. Excitation strength can be quantified by the so-called nutation angle $\theta = \gamma|B_1|t_p$ of each RF pulse. Let us define $0 < \eta < 1$ as the asymmetry parameter of the electric field gradient (EFG) tensor in the principal axis system (PAS) fixed on the nucleus, as is conventional in NQR. For powder samples of spin-1 ($I = 1$) nuclei with $\eta \neq 0$, the response function is given by

$$s_{exc}(\theta) = \sqrt{\frac{\pi}{2\theta}} J_{3/2}(\theta). \tag{10}$$

Here $J_{3/2}$ is the Bessel function of the first kind and order 3/2 [22]. The maximum signal amplitude for powder samples is approximately 0.426 after normalization, and occurs when the nutation angle $\theta \approx 120^\circ$.

The absolute amplitude of the signal generated during an NMR experiment can be estimated using well-known formulas [23]. The derivation for NQR proceeds in a similar way. First we estimate the magnetization density induced by an excitation pulse with a nutation angle of θ. Under the assumption of weak irradiation of the sample, the result is [24]:

$$M_0 = s_{exc}(\theta)\rho_s \frac{\gamma\hbar^2\omega_0}{kT_s}\left(\frac{I(I+1) - mm'}{2I+1}\right), \quad \text{where } \rho_s = N \times N_A \times \rho, |m - m'| = 1. \tag{11}$$

Here ρ_s is the number of spins per cm^3, which is the product of N (the number of spins per molecule), N_A (the number of molecules per gram), and ρ (sample density in grams per cm^3). While calculating the amplitude of a single line in the spectrum, N should be replaced with 1. In addition, γ is the gyromagnetic ratio, $\hbar$ is Planck's constant, ω_0 is the resonant frequency, kT_s is the product of the Boltzmann constant and sample temperature, and m and m' are the quantum numbers of the nuclear states before and after the transition. Finally, I is the total angular momentum (nuclear spin); when $I = 1$, the formula reduces to [25]

$$M_0 = s_{exc}(\theta)\rho_s \frac{\gamma\hbar^2\omega_0}{3kT_s}. \tag{12}$$

If B_1 is considered to be reasonably homogeneous over the sample volume and M_0 lies in the xy-plane, the induced emf on the coil can be simplified from a three-dimensional calculation to a simple analytical procedure, as described below. Assuming that the coil

acts as both the transmitter and receiver, the coupling between the spin precession signal and the coil can be quantified by a mutual inductance M. Thus the induced voltage in the coil in sinusoidal steady state is given by

$$V_0 = -\frac{d\phi_{21}}{dt} = -\omega_0 MI\cos(\omega_0 t). \tag{13}$$

Here ϕ_{21} is the magnetic flux generated within the coil during reception by the precessing nuclear spins. This equation is valid when the signal is narrow-band, i.e. the NQR line width is much smaller than the resonant frequency ω_0. This is usually the case.

The magnetic moment $\vec{\mu}$ of a loop of area A carrying a current I, according to the equation $E = -\vec{\mu}\cdot\vec{B}$ for magnetic field energy, is simply $I\vec{A}$. Thus, if we define the effective area for the spin magnetic moment as A_0, the Eq. (13) can be written as:

$$V_0 = -\omega_0 \frac{M\mu}{A_0}\cos(\omega_0 t). \tag{14}$$

Furthermore, the reciprocity theorem for electromagnetic fields ensures that $M_{12} = M_{21}$. Using this fact, we have

$$V_0 = -\omega_0 \frac{M\mu}{A_0}\cos(\omega_0 t) = -\omega_0 \frac{\phi_{12}}{A_0 I_1}\mu\cos(\omega_0 t). \tag{15}$$

We can now use the definition of flux to write $\phi_{12} = B_1 A_0$ as the flux generated within the spins by the coil during transmission. As a result we get

$$V_{coil} = V_0 V_s = -\omega_0\left(\frac{B_1}{I_1}\right)M_0 V_s\cos(\omega_0 t), \tag{16}$$

where V_s is the volume occupied by the particular species of interest within the sample. The B_1/I_1 term is a measure of coupling strength between the coil and the sample. For an long solenoid, we can easily use Ampere's Law to find that $B_1/I_1 = \mu N/l$, where μ is the permeability, N is the number of turns, and l is the length of the coil. A more accurate calculation can be carried out by taking into account the fact that the solenoid coil is not infinitely long, and thus the magnetic field strength decreases when approaching both ends of the coil. Along the center of the coil (assumed to be the x-axis), B_1/I_1 can be represented as

$$\frac{B_1(x)}{I_1} = \frac{\mu_0 N}{4\ell}\left(\frac{2x+\ell}{\sqrt{(2x+\ell)^2+D^2}} - \frac{2x-\ell}{\sqrt{(2x-\ell)^2+D^2}}\right). \tag{17}$$

Here D is the diameter of the coil. Wheeler's inductance formula may be used to estimate the resulting coil inductance L_{coil} [26]. Next we need to consider the transfer function of the matching network. The voltage at the output of the network V_{rx}, i.e., across the receiver terminals, is given by

$$V_{rx} = \frac{1}{2}\frac{V_{coil}}{j\omega L_{coil}}\left(Z_0 - \frac{1}{sC_2}\right). \tag{18}$$

Here Z_0 is the matched impedance (usually 50 Ω). Furthermore, if we ignore the power loss in the matching network, this equation can be written as

$$V_{rx} \approx \frac{V_{coil}}{2}\sqrt{\frac{Z_0}{R_{coil}}}. \tag{19}$$

Here R_{coil} is the series resistance of the coil at the operating frequency ω_0. Finally, the effect of the digital filter is not negligible. All the formulas derived so far ignore signal decay, so we would like to derive a filter that optimally estimates initial signal amplitude (at $t = 0$) from the acquired echoes. We define $w(t)$ to be the rectangular signal acquisition window (of length t_{acq}) for each echo, and $W(\omega)$ to be its Fourier transform. Ignoring noise for the moment, the measured spectrum of the k-th echo signal is then given by

$$S_a(\omega, kt_E) = S(\omega, kt_E) * W(\omega), \tag{20}$$

where $S(\omega, kt_E)$ is the true spectrum (with no windowing), and t_E is the echo period. Taking an inverse Fourier transform, we find that the windowed time-domain echo $s_a(\Delta t, kt_E) = s(\Delta t, kt_E)w(\Delta t)$ is given by

$$s_a(\Delta t, kt_E) = \int_{-\infty}^{+\infty} S_a(\omega, kt_E)e^{j\omega\Delta t}d\omega. \tag{21}$$

Here $-t_{acq}/2 < \Delta t < t_{acq}/2$ denotes time within each acquisition window. Moreover, in this range, we know that the effects of inhomogeneous signal decay (T_2^* relaxation) are removed at the peaks of echoes, which are assumed to occur at $\Delta t = 0$. Thus, the quantity

$$s_a(0, kt_E) = \int_{-\infty}^{+\infty} S_a(\omega)d\omega \tag{22}$$

is a good estimate of the amplitude of the NQR signal at time kt_E without T_2^* decay [27]. The function $s_a(0, kt_E)$ is then fitted to an exponential or bi-exponential function to estimate the initial signal amplitude $s_a(0,0) \equiv V_{rx}G(\omega_0)$, thus removing the effects of both T_2^* and $T_{2,eff}$ decay; here $G(\omega_0)$ is the voltage gain of the receiver. This estimation procedure uses a version of apodization; a slightly different version is discussed in the next appendix.

By combining Eqs. (11)–(22), we can now estimate N_s, the total number of nuclei of the species of interest within the sample, entirely from known quantities. The result is

$$N_s = \rho_s V_s = \frac{s_a(0,0)}{G(\omega_0)}\sqrt{\frac{\omega_0 L_{coil}}{Z_0 Q}}\frac{6kT_s}{\gamma\hbar^2\omega_0^2}\left(\frac{B_1}{I_1}\right)^{-1}\frac{1}{s_{exc}(\theta)}. \tag{23}$$

This equation is the basis of quantitative NQR measurements. In practice, it is complicated by the fact that B_1 intensity within the sample is not uniform, which results in a distribution of nutation angles θ. For solenoids the variation is mostly longitudinal as shown in Eq. (17), so it is sufficient to perform a one-dimensional integral over the sample length. The result is

$$N_s = \frac{s_a(0,0)}{G(\omega_0)}\sqrt{\frac{R_{coil}}{Z_0}}\frac{6kT_s}{\gamma\hbar^2\omega_0^2}\left[\frac{l_s}{\int_{-l_s/2}^{l_s/2} s_{exc}(\theta(x))\left(\frac{B_1(x)}{I_1}\right)dx}\right]. \tag{24}$$

Here $\theta(x) \equiv \gamma B_1(x)t_p$, while l_s and t_p are the lengths of the sample and the RF pulses, respectively.

Appendix B. Matched filtering

B.1. Matched filtering for white noise. Derivation of Eq. (6)

A matched filter is essential in low-power experiments to optimize the SNR and make the received signal suitable for detection. The matched filter is a linear time-invariant filter with an impulse response $h(\Delta t)$ that operates on the noisy echo signal $r(\Delta t) = s_a(\Delta t) + n(\Delta t)$, where $n(\Delta t)$ denotes additive noise. The time-domain output $y(\Delta t)$ of the filter is the sum of two convolution integrals:

$$y(\Delta t) = \int_{-\infty}^{+\infty} s_a(\tau)h(\Delta t - \tau)d\tau + \int_{-\infty}^{+\infty} n(\tau)h(\Delta t - \tau)d\tau, \tag{25}$$

where the first term is the signal component, and the second one is the noise component. Let us assume that $n(\Delta t)$ is Gaussian white noise that is uncorrelated with the signal, which is usually a good assumption as long as i) the bandwidth of the front-end is broader than that of the signal, and ii) there is no significant external RF

interference (RFI) near the operating frequency ω_0. In this case the SNR in terms of power is given by

$$SNR(\Delta t) = \frac{\left[\int_{-\infty}^{+\infty} s_a(\tau)h(\Delta t-\tau)d\tau\right]^2}{\frac{N_0}{2}\int_{-\infty}^{+\infty}\left|h^2(\tau)\right|d\tau}. \tag{26}$$

Applying the Cauchy-Schwartz inequality, we know that

$$SNR(\Delta t) \leqslant \frac{\int_{-\infty}^{+\infty}|s_a^2(\tau)|d\tau\int_{-\infty}^{+\infty}\left|h^2(\tau)\right|d\tau}{\frac{N_0}{2}\int_{-\infty}^{+\infty}\left|h^2(\tau)\right|d\tau} \leqslant \frac{2}{N_0}\int_{-\infty}^{+\infty}|s_a^2(\tau)|d\tau. \tag{27}$$

Here N_0 is the power spectrum density (PSD) of $n(\Delta t)$. We are interested in SNR maximum signal. The SNR is maximized when the "less than equal to" sign in the expression above becomes "equal to". This occurs when $h(\Delta t-\tau) = cs_a^*(\tau)$, i.e., $h(\tau) = cs_a^*(\Delta t-\tau)$ where c is a real constant and $s_a^*(\Delta t-\tau)$ is the complex conjugate of $s_a(\Delta t-\tau)$. For convenience, let us maximize SNR in the middle of the acquisition window, i.e., at $\Delta t = 0$. In this case $h(\tau) = cs_a^*(-\tau)$, i.e., is the complex conjugate of a scaled and time-reversed version of the noiseless echo shape $s_a(\tau)$. *The simplification also replaces the convolution with multiplication by a weighting function, i.e., apodization.* The form of this function (the matched filter) can be estimated from experimental data sets by averaging the shapes of many echoes. However, the averaging process makes the expected value of $h(\tau)$ dependent on the decay time constant $T_{2,eff}$:

$$\overline{h(\tau)} = \frac{cs_a^*(-\tau,0)}{N_E}\sum_{k=1}^{N_E}e^{-kt_E/T_{2,eff}}. \tag{28}$$

where $c = 1/\sqrt{\int_{-\infty}^{+\infty}|s_a(\tau,0)|^2d\tau}$ and $s_a(\tau,0)$ is the echo shape extrapolated to $t = 0$, as before. As a result, the calculated echo amplitudes will also be weighted by $T_{2,eff}$:

$$\begin{aligned} y_s(k) &\approx \int_{-\infty}^{+\infty} s_a(\tau,kt_E)\overline{h(-\tau)}d\tau \\ &= \frac{c\sum_{k=1}^{N_E}e^{kt_E/T_{2,eff}}}{N_E}e^{-kt_E/T_{2,eff}}\int_{-\infty}^{+\infty}|s_a(\tau,0)|^2d\tau. \end{aligned} \tag{29}$$

However, it is desired that the initial amplitude is dependent solely on the total number of excited nuclear spins, instead of $T_{2,eff}, T_E$, and N_E. This can be achieved by applying another layer of matched filtering, which weighs each noisy received echo $r(t) = s_a(t) + n(t)$ by its expected SNR, as follows:

$$\begin{aligned} h(\tau) &= \frac{c\sum_{k=1}^{N_E}r^*(-\tau,kt_E)e^{-kt_E/T_{2,eff}}}{\sum_{k=1}^{N_E}e^{-kt_E/T_{2,eff}}e^{-kt_E/T_{2,eff}}} \\ &= \frac{c\sum_{k=1}^{N_E}\left[s_a^*(-\tau,kt_E)+n^*(-\tau)\right]e^{-kt_E/T_{2,eff}}}{\sum_{k=1}^{N_E}e^{-2kt_E/T_{2,eff}}} \\ &\Rightarrow \overline{h(\tau)} = \frac{c\sum_{k=1}^{N_E}s_a^*(-\tau,kt_E)e^{-kt_E/T_{2,eff}}}{\sum_{k=1}^{N_E}e^{-2kt_E/T_{2,eff}}}. \end{aligned} \tag{30}$$

Thus the expected echo amplitudes are given by:

$$\begin{aligned} y_s(kt_E) &\approx \int_{-\infty}^{+\infty}s_a(\tau,0)e^{-kt_E/T_{2,eff}}\overline{h(\tau)}d\tau = ce^{-kt_E/T_{2,eff}}\int_{-\infty}^{+\infty}|s_a(\tau,0)|^2d\tau \\ &= e^{-kt_E/T_{2,eff}}\sqrt{\int_{-\infty}^{+\infty}|s_a(\tau,0)|^2d\tau}. \end{aligned} \tag{31}$$

B.2. Matched filtering for non-white noise. Derivation of Eq. (7)

In the presence of non-white noise, we need a pre-whitening filter $H_W(\omega)$ in addition to the usual filter described in the last section. The job of the pre-whitening filter is to convert the colored noise PSD $N(\omega)$ into white noise. Such a whitening filter can be defined as

$$H_W(\omega) = \sqrt{\frac{N_{out}}{N(\omega)}}, \tag{32}$$

where N_{out} is the constant (frequency-independent or white) noise PSD at the output of the filter. After the whitening operation, the signal spectrum is given by $S_a(\omega)H_W(\omega)$, so the required matched filter is

$$H_M(\omega) \equiv [S_a(\omega)H_W(\omega)]^* = S_a^*(\omega)H_W^*(\omega). \tag{33}$$

The whitening and matched filters can now be combined into a single, modified matched filter that is given by

$$H'_M(\omega) \equiv H_W(\omega)H_M(\omega) = S_a^*(\omega)|H_W(\omega)|^2 = N_{out}\left(\frac{S_a{}^*(\omega)}{N(\omega)}\right). \tag{34}$$

In order to implement this filter, one obviously needs to know the noise PSD. This may be estimated from the output noise of the receiver with no signal, i.e., without applying any RF pulses. The detected signal amplitude is now given by

$$Y_M(\omega) = S_a(\omega)H'_M(\omega) = \frac{N_{out}|S_a(\omega)|^2}{N(\omega)}. \tag{35}$$

$$\begin{aligned} y_M &= \int_{-\infty}^{\infty}Y_M(\omega)d\omega = N_{out}\int_{-\infty}^{\infty}\frac{|S_a(\omega)|^2}{N(\omega)}d\omega \\ &= N_{out}\int_{-\infty}^{\infty}|SNR(\omega)|^2d\omega. \end{aligned} \tag{36}$$

Appendix C. Supplementary material

Supplementary data associated with this article can be found, in the online version, at http://dx.doi.org/10.1016/j.jmr.2017.03.011.

References

[1] E.D. Kantor, Trends in dietary supplement use among us adults from 1999–2012, Jama 316 (14) (2016) 1464–1474.
[2] R.J. Maughan, Contamination of dietary supplements and positive drug tests in sport, J. Sports Sci. 23 (9) (2005) 883–889.
[3] ComsumerLab.com, Product review: protein powders & drinks, Apr 2016. <https://www.consumerlab.com/reviews>.
[4] U.S. Food and Drug Administration, Two New Jersey dietary supplement companies and their principals found guilty of criminal contempt, Nov 2011. <http://www.fda.gov/ICECI/CriminalInvestigations/ucm282730.htm>.
[5] G.A. Green, D.H. Catlin, B. Starcevic, Analysis of over-the-counter dietary supplements, Clin. J. Sport Med. 11 (4) (2001) 254–259.
[6] A.B. Champagne, K.V. Emmel, Rapid screening test for adulteration in raw materials of dietary supplements, Vib. Spectrosc. 55 (2) (2011) 216–223.
[7] J. Luypaert, D.L. Massart, Y.V. Heyden, Near-infrared spectroscopy applications in pharmaceutical analysis, Talanta 72 (3) (2007) 865–883.
[8] C.J. Strachan, T. Rades, K.C. Gordon, J. Rantanen, Raman spectroscopy for quantitative analysis of pharmaceutical solids, J. Pharm. Pharmacol. 59 (2) (2007) 179–192.
[9] S. Wartewiga, R.H.H. Neubert, Pharmaceutical applications of mid-IR and Raman spectroscopy, Adv. Drug Deliv. Rev. 57 (8) (2005) 1144–1170.
[10] A. Cifuentes, Food Analysis: Present, Future, and Foodomics, ISRN Analytical Chemistry, 2012.
[11] J.B. Miller, Nuclear Quadrupole Resonance Detection of Explosives, Elsevier, Netherlands, 2007, pp. 157–198.
[12] J. Fraissard, O.L. (Eds.), Explosives Detection using Magnetic and Nuclear Resonance Techniques (NATO Science for Peace and Security Series B: Physics and Biophysics), Springer, 2009.
[13] S. Mandal, Y.-Q. Song, Two-dimensional NQR using ultra-broadband electronics, J. Magn. Reson. 240 (2014) 16–23.
[14] S. Mandal, S. Utsuzawa, D.G. Cory, M.D. Hürlimann, M. Poitzsch, Y.-Q. Song, An ultra-broadband low-frequency magnetic resonance system, J. Magn. Reson. 242 (2014) 113–125.
[15] G.V. Mozzhukhin, B.Z. Rameev, N. Doğan, B. Aktaš, The Two-frequency Multipulse Sequence in Nuclear Quadrupole Resonance of N-14 Nuclei, Springer, Netherlands, 2009, pp. 205–230.

[16] K. Sauer, B. Suits, A. Garroway, J. Miller, Three-frequency nuclear quadrupole resonance of spin-1 nuclei, Chem. Phys. Lett. 342 (34) (2001) 362–368.
[17] T.A. Heddle, A method of designing a compensated solenoid giving approximately uniform field, Br. J. Appl. Phys. 3 (3) (1952) 95.
[18] K.J. Overshott, I.R. Smith, A solenoid with a nearly uniform axial magnetic field, J. Sci. Instrum. 41 (8) (1964) 507.
[19] J. LuŽnik, J. Pirnat, V. JazbinŠek, Z. Trontelj, T. Apih, A. GregoroviČ, R. Blinc, J. Seliger, Polarization Enhanced NQR Detection at Low Frequencies, Springer, Netherlands, Dordrecht, 2009, pp. 41–56.
[20] K.R. Thurber, K.L. Sauer, M.L. Buess, C.A. Klug, J.B. Miller, Increasing ^{14}N NQR signal by ^{1}H-^{14}N level crossing with small magnetic fields, J. Magn. Reson. 177 (1) (2005) 118–128.
[21] C. Chen, F. Zhang, J. Barras, K. Althoefer, S. Bhunia, S. Mandal, Authentication of medicines using nuclear quadrupole resonance spectroscopy, IEEE/ACM Trans. Comput. Biol. Bioinformatics 13 (3) (2016) 417–430.
[22] Y. Lee, Spin-1 nuclear quadrupole resonance theory with comparisons to nuclear magnetic resonance, Concept. Magnetic Res. 14 (3) (2002) 155–171.
[23] D.I. Hoult, R.E. Richards, The signal-to-noise ratio of the nuclear magnetic resonance experiment, J. Magnetic Res. 24 (1) (1976) 71–85.
[24] H.G. Dehmelt, Nuclear quadrupole resonance, Am. J. Phys. 22 (3) (1954) 110–120.
[25] J.B. Miller, Nuclear quadrupole resonance detection of explosives: an overview, Proc. SPIE 8017 (2011), pp. 801715–801715–7.
[26] H.A. Wheeler, Simple inductance formulas for radio coils, Proc. Inst. Radio Eng. 16 (10) (1928) 1398–1400.
[27] S. Mandal, Y.-Q. Song, Heteronuclear J-coupling measurements in grossly inhomogeneous magnetic fields, J. Magn. Reson. 255 (2015) 15–27.